Schlieren Imaging of a Hypersonic Wave Rider Model in a Hypersonic Arcjet Tunnel

Carson M. Waddell *, Damiano Baccarella †
University of Tennessee, Knoxville, Tennessee, 37996

In this work, Schlieren imaging was used to track and identify the formation of shocks on a scaled-down model of a hypersonic wave rider aircraft. The model is tested at two different angles of attack, 0° and 10.38°, in a low-enthalpy Mach 6 flow produced by an altered arcjet facility to act as a traditional blowdown tunnel with a pure nitrogen (N_2) working gas. Schlieren images were acquired using a high-speed camera to observe the oblique shocks that form at the leading edge of the vehicle, while additionally tracking the aerodynamic effects that lead to the scramjet inlet of the model. At each of the tested angles of attack, a secondary shock is seen interacting with the primary oblique shock towards the back of the vehicle. For both of the tested angles of attack, the formation of a bow shock was observed at the leading edge of the inlet. At the higher angle, the intensity of this bow shock increases while the initial oblique shock propagates further above the lower edge of the inlet than what is observed in the no angle of attack case.

I. Introduction

For decades, researchers have used Schlieren imaging in ground-based testing facilities to identify and track boundary layers, shock formations, expansion fans, and many other supersonic phenomena [1]. Schlieren imaging, as a form of flow visualization, has a wide range of applications in supersonic and hypersonic ground testing, from studying high-speed plasma jets to capturing characteristics of hypersonic flow in experiments [2–4]. Schlieren is primarily used as a measurement technique to collect qualitative data. Whereas in recent years, with improvements in camera quality and frame rates, some experiments have acquired quantitative data [5]. Schlieren imaging is implemented in supersonic and hypersonic wind tunnels across the country to supplement many of their everyday experiments with non-intrusive flow visualization. The 10×10 foot supersonic wind tunnel at NASA's Glenn Research Center and the 4-foot Unitary Plan facility at NASA's Langley Research Center are two examples of large-scale ground-based testing facilities that have developed permanent schlieren imaging setups that can be used for many, if not all, of their experimental testing. [6, 7]. The application of Schlieren in these facilities have showed promising diagnostic contributions to a wide variety of reentry vehicles and hypersonic aircraft models and have served a crucial role in programs such as the Space Shuttle and more recently the development of the Orion capsule.

Testing and modeling shock interactions in supersonic and hypersonic flight is essential to understanding a vehicle's aerodynamic and thermodynamic performance. Proper oblique shock attachment near the nose of a scramjet vehicle is essential in maintaining proper inlet compression efficiency in flight. The proper and sustained oblique and bow shock formation in the inlet region ensure proper and sustained ignition while avoiding unstart [8]. As a result of the high manufacturing costs associated with hypersonic vehicle development, full-scale in-flight testing continues to be an infeasible effort to analyze performance. A more practical solution is to conduct testing and performance analysis with scaled-down models in hypersonic wind tunnels that simulate high-altitude flight conditions. The use of hypersonic wind tunnels when coupled with high-speed Schlieren imaging allows for the testing and analysis of new vehicles before full-scale deployment.

This work focuses on the implementation of high-speed Schlieren imaging to qualitatively evaluate the various shocks formed on a scaled-down hypersonic wave rider model. These tests were conducted in a hypersonic arcjet tunnel, set in an arc-off configuration, to produce Mach 6 cold flow as described in Sec. II.A. A 3D printed hypersonic wave rider model as described in Sec. II.B, was designed and manufactured to be tested at varying angles of attack to study shock formation near the engine inlet. Sec. II.C describes the Z-Type Schlieren imaging setup that was implemented using a high-speed camera. The results are analyzed in Sec. III, where figures are provided to compare the two different angles of attack and their effects on shock formations. Concluding remarks are made in Sec. IV.

*Undergraduate Research Assistant, Mechanical Aerospace and Biomedical Engineering Department, AIAA Student Member 1539246.
†Assistant Professor, Mechanical Aerospace and Biomedical Engineering Department, AIAA Senior Member.

II. Experimental Setup

A. Tennessee High Enthalpy Tunnel

The Tennessee High Enthalpy Tunnel (TennHET), located at the University of Tennessee, Knoxville, is an arc-heated wind tunnel used to produce the high-temperature flow experienced in Mach 6 flight conditions [9]. The facility is currently configured to operate in a pulsed mode, in which the duration for each test is limited to a maximum of one second, with typical tests ranging around 500 ms. For these tests, 2 fast-opening solinoid valves are used to release a pure nitrogen (N_2) working gas initially pressurized to 50 psig, into the arc-heater which was set to an arc-off configuration resulting in an ambient stagnation temperature. The mass flow rate through the nozzle was measured to be 21.9 g/s. The Mach 6 converging-diverging nozzle selected for testing has a conical geometry with an exit diameter of 85 mm. Kulite pressure sensors located in the plenum chamber of the tunnel allow stagnation pressure measurements to be recorded. The free jet design at the nozzle exit allows the flow to expand into a 750 mm diameter cylindrical test section, outfitted with six 250 mm circular view ports for optical access. The base of the test section contains a 2-dimension electronically controlled translation system for mounting and injecting various probes and models in and out of the core flow. Using this stage, a Pitot probe can be precisely positioned to the same reference location of the tested model to evaluate the freestream conditions by measuring the post-normal shock stagnation pressure.

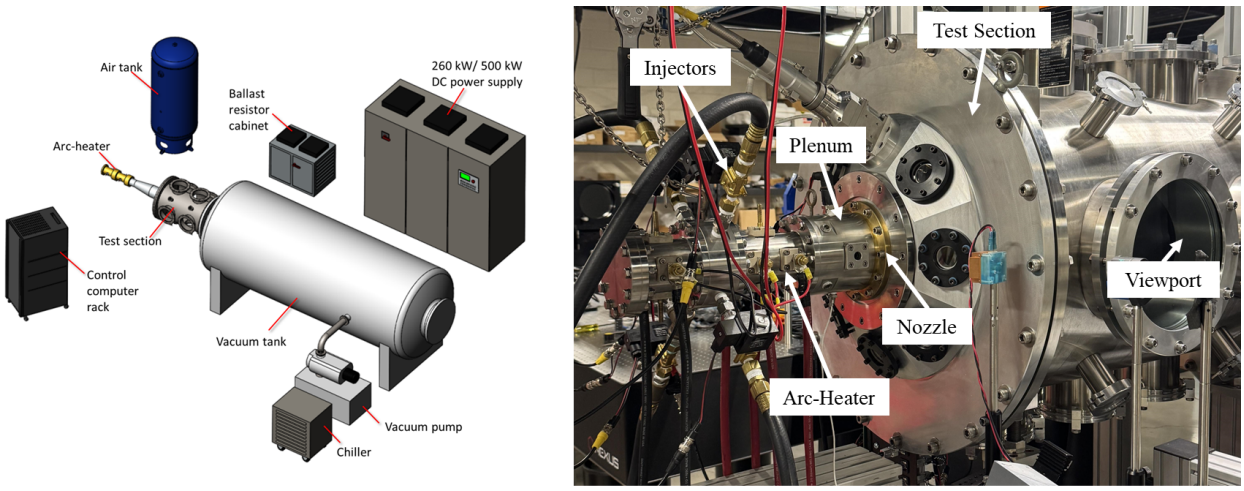

Fig. 1 (a) CAD overview of the main component for the arcjet tunnel. (b) Labeled image of the arc-heater and test section.

B. Hypersonic Wave Rider Modeling and Construction

The model used in this work was based on a hypersonic wave rider vehicle. Two iterations of the model were made with changes to the inlet and nose shape being the primary areas of revision. One of these revisions was to reduce the deflection angle of the initial oblique shock that leads to the inlet. To achieve this, the radius of curvature of the contoured surface was increased, resulting in a larger inlet cross-sectional area to better the chance of the oblique shock propagating into the inlet. The final model has been 3D printed using polylactic acid with a 0.4 mm tolerance. Due to this tolerance, there were limitations on the addition of smaller details and surface smoothness.

The scaled-down model, as seen in Fig. 2, has dimensions of $19 \times 23 \times 123$ mm representing the height, width, and length, respectively. Starting at the nose of the vehicle, a curved surface with a radius of 30.4 mm leads into an inlet with a cross-sectional area of 87.0 mm^2. The distance from nose to inlet is 38.5 mm. The model was axially centered and positioned 76.2 mm from the nozzle exit. In this study, two different variations of angles of attack were implemented, $\alpha = 0°$ and 10.38°.

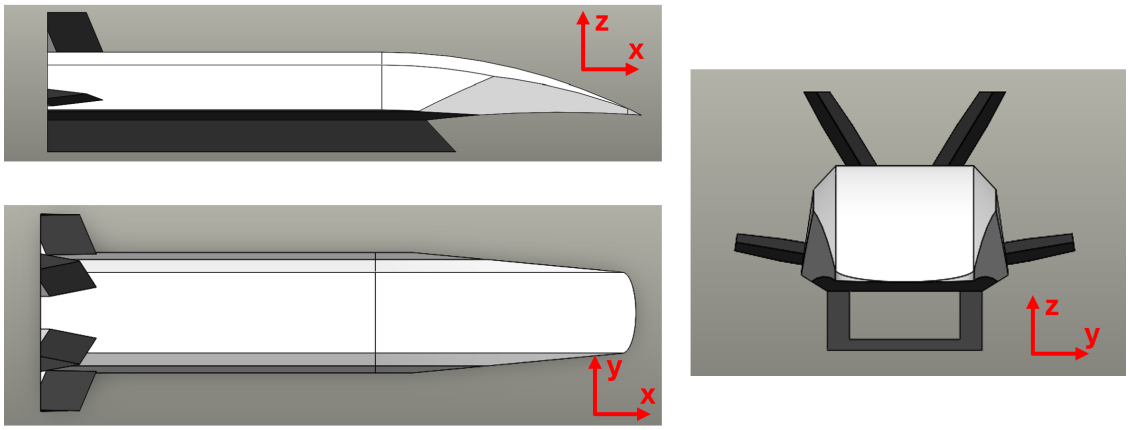

Fig. 2 Hypersonic wave rider CAD model displaying the front, top, and side views.

C. Z-Type Schlieren Setup

An incoherent white-light source, designed and created at the University of Tennessee, was operated at a current of 1.5 amps using a controlled power supply. The light from this source is focused using a 75 mm Plano-Convex focusing lens onto an adjustable pinhole at the focal length of the first spherical concave mirror as shown in Fig. 3. The 6 inch diameter mirror, with a focal length of 4 ft, is used to collimate light through the test section. The test section contains two glass windows that allow the collimated light to pass through and proceed to the second 6 inch spherical concave mirror. This mirror redirects the light onto a razor blade located at the 4 ft focal distance from the mirror. The razor blade cuts off half of the refocused light, which is then received by the Photron Nova X16 high-speed camera. The camera was configured with a 100 mm Macro 2× lens attached and mounted outside the test section. The camera was set to a frame rate of 44,000 Hz and a pixel resolution of 640 × 576 to produce a frame size of 6.67 × 6 inches.

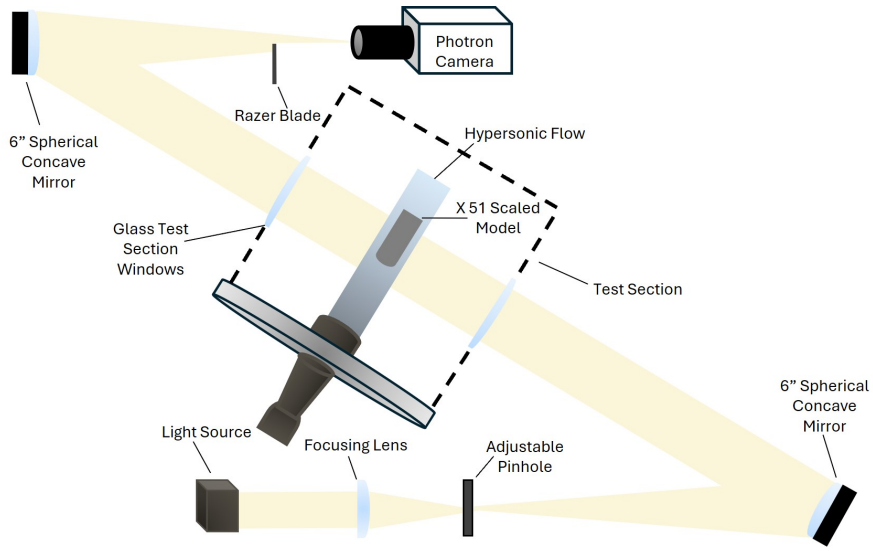

Fig. 3 Schlieren setup used to image flow conditions in the test section of the tunnel facility.

A total of 35,000 frames were recorded for each of the two different angles of attack, providing 90.8 ms of observation over the tunnel's working condition. An exposure time of 10 μs correlated to a spatial resolution of 25 mm when a freestream flow velocity of 2500 m/s was assumed. In addition to recording each test, background images were taken to perform subtraction.

III. Schlieren Imaging Results

Images acquired at various instances during testing of the hypersonic wave rider model are displayed in Fig. 4 for the two different angles of attack. The top row of images in Fig. 4 represents the first tested angle of attack at 0°, where, moving from left-to-right, the first image is representative of the referenced tunnel operating time (t_0) of 113.6 ms. The following images that proceed on this row correspond to uniform changes in time (Δt) of 22.7 ms. This is the same for the bottom row of Fig. 4, which shows the other test angle of attack at 10.38°. We can clearly see across this temporal range that there are minimal changes in the observed shock formation over time. This remains the case even when there is minor detected unsteadiness in the freestream flow, as we can see by comparing the images in the top row of Fig. 4. As a result of the consistency across the test duration, the produced shock features, such as the oblique shocks, were able to be analyzed and compared to the time-averaged freestream conditions and the variation in angle of attack.

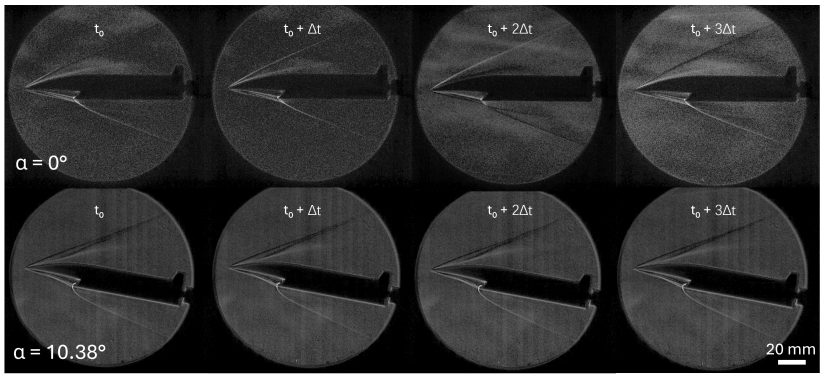

Fig. 4 4 images selected from two separate runs the top images being α = 0° and the bottom images being α = 10.38°. The values of $t_\circ$ and Δt are 113.6 ms and 22.7 ms respectively.

These two angle of attack values were chosen to determine the effect angle of attack, α, has on shock formation. Both angles of attack show oblique shocks generated off the nose of the vehicle, and what appears to be multiple shocks that propagate towards the engine inlet of the model. The acquired images provided sufficient contrast and detail for a visual analysis to be made. The oblique shock for the 10.38° angle of attack has a more pronounced curve near the engine inlet than the vehicle angled at 0°. An increase in the contrast and size of the bow shock near the model's inlet is also evident at the higher α value.

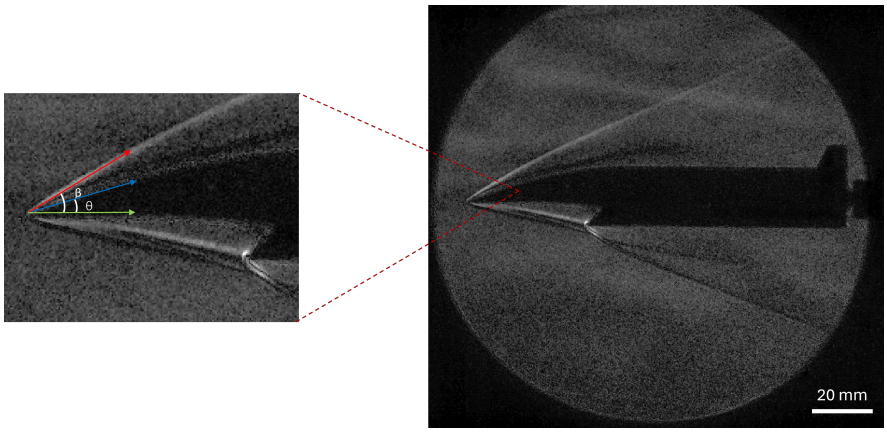

Fig. 5 Schlieren imaging of a hypersonic wave rider model with α = 0° with secondary imaging focusing on the vehicle's nose and inlet section.

In Fig.5, a clear oblique shock attachment can be seen near the nose of the vehicle when α is zero. Assuming shock attachment to the tip of the nose and a near-uniform deflection angle θ along the initial 10 mm of the nose, the $\theta - \beta - M$ relation

$$\tan\theta = 2\ \cot\beta \left[\frac{M_1^2 \sin^2\beta - 1}{M_1^2(\gamma + \cos 2\beta) + 2}\right], \tag{1}$$

was used to determine the upstream Mach number from the measured oblique shock angle β. The specific heat ratio, γ, is set to 1.4 due to the working gas being pure N_2. Using geometric relations, θ was found to be 21.80° while β was 32.35°. These calculations yielded a predicted upstream Mach number of 4.78 ± 0.5, where the uncertainty was the result of the resolution of the images and the Schlieren imaging being a path-integrated measurement.

This measured Mach number was significantly lower because of the larger shock angle than was anticipated to be produced by the tunnel's Mach 6 nozzle. As further result of this the lower oblique shock, that was designed to intersect the engine inlet, proceeded below the inlet, thus essentially reducing the compression efficiency.

The tests performed at a higher angle of attack, 10.38°, were analyzed slightly more in detail than the previous case, as seen in Fig. 6. In this figure, location (a) highlights the attachment of the oblique shock on the nose of the vehicle. Location (b) emphasizes the curvature of this oblique shock as it approaches the engine inlet. Location (e) highlights the formed bow shock at the leading edge of the engine inlet where a stagnation point is anticipated to occur. The interaction between this bow shock and the curved oblique shock is also detected directly in front of the inlet surface. Location (c) points to a potential secondary shock formation slightly farther back along the vehicle compared to the oblique shock formed near the nose. This shock eventually interacts with the oblique shock attached to the nose further down the vehicle at location (d). Slightly above this shock interaction, we can additionally observe the flow boundary as identified by position (f).

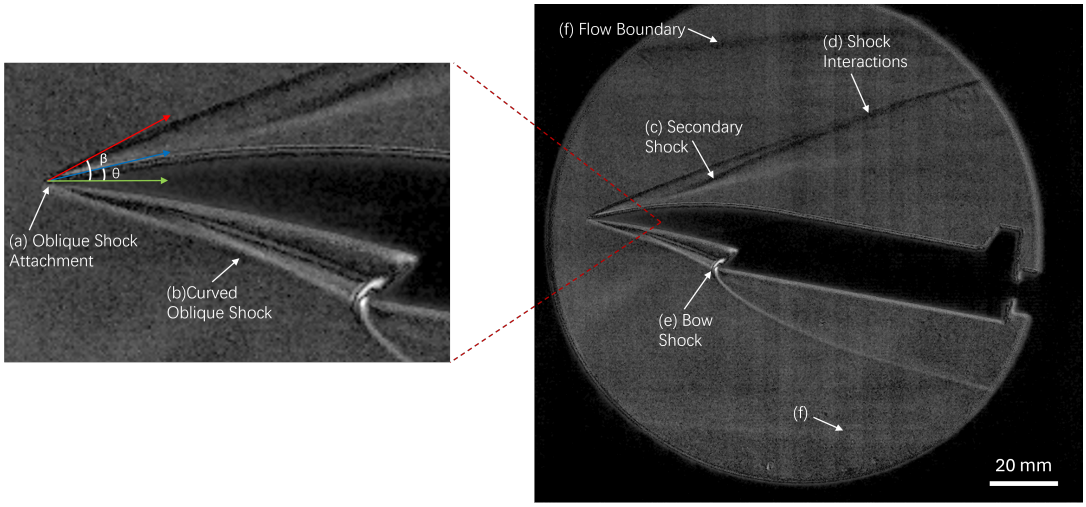

Fig. 6 Schlieren image of a hypersonic wave rider model with secondary image focused on nose portion of the vehicle.

To further analyze, the values of θ and β were found again for the higher α value as shown in Fig. 6. Under the same assumptions as in the previous case, the $\theta - \beta -$ M relation was used again to calculate the predicted upstream Mach number. The values of θ and β of 15.95° and 26.57°, respectively, resulted in a calculated mach number of M = 4.47 ± 0.5, this value compared to the Mach number associated with $\alpha = 0°$ demonstrates the consistency of deriving upstream Mach number from the $\theta - \beta -$ M relation. Contrary to the lower angle of attack, the lower oblique shock in the higher α case appears to propagate directly into the inlet, with no shock being observed beyond this region, suggesting a better compression efficiency. This ultimately allows for the stronger bow shock formation that is highlighted in Fig. 6.

Comparison is made between the derived Mach numbers from the image analysis and the measured Mach number from a pitot probe positioned at the same distance from the nozzle exit as the vehicle (76.2 mm) [10]. This additional measurement is performed by taking the ratio between the post-shock stagnation pressure of the probe, p_s, and the initial stagnation pressure of the freestream, p_o, measured in the plenum chamber. Applying the normal shock equation

$$\frac{p_s}{p_o} = \left[\frac{(\gamma+1)M^2}{(\gamma-1)M^2+2}\right]^{\frac{\gamma}{\gamma-1}} \left[\frac{(\gamma+1)}{2\gamma M^2-(\gamma-1)}\right]^{\frac{\gamma}{\gamma-1}} \tag{2}$$

the Mach number, M, can be derived. Additionally, γ is set to 1.4 similarly to what was performed in Eq.(1).

These pitot probe measurements resulted in a $p_s/p_o = 0.0145$, corresponding to an upstream Mach number of M = 7.09. Comparing this Mach number with that calculated at $\alpha = 0°$ yields a percent error of 32.58 %, whereas comparing to the Mach number calculated at $\alpha = 10.38°$ results in a percent error of 36.95 %.

IV. Conclusion

Schlieren imaging was performed on a hypersonic wave rider vehicle model to track and analyze shock formations and how they change at various angles of attack, 0° and 10.38°. Experiments performed in a Mach 6 tunnel had a strong contrast of shock formations that remained consistent throughout the duration of the test. The clarity of the images allowed for the deflection angle and the oblique shock angle to be measured at both angles of attack. The upstream Mach number for $\alpha = 0°$ and $\alpha = 10.38°$ was found to be 4.78 ± 0.5 and 4.47 ± 0.5, respectively. The determined mach numbers were compared to measurements derived from a pitot probe at the same location in the freestream. This measurement resulted in a Mach number of 7.09, leading to a 32.58% error to what was determined at the lower angle of attack, and a 36.95% error for the higher angle of attack. At the lower angle of attack, the lower oblique shock does not intersect with the engine inlet, whereas at the higher angle of attack, the shock successfully intersects with the inlet due to the reduced deflection angle. This intersection occurrence is ideal for maintaining a higher compression efficiency at the inlet. At the higher angle of attack, a more intense bow shock was identified than was observed for the lower angle case. This is mainly due to the fact that more of the leading edge of the inlet is exposed to the high-velocity freestream than at the zero angle of attack, where the edge is fully encompassed by the initial oblique shock.

Further investigation will need to be performed to identify the potential causation in the large discrepancy between the Mach number determined from the Schlieren images and the pitot probe measurement. To pursue this, additional Schlieren experiments will be performed using a smaller field of view to significantly improve the spatial resolution, thus reducing the error in the measured angles. Alterations to vehicle geometry will include simplifying the model to a planar-shaped geometry, in which the same cross-sectional area will remain constant along the y-direction. Additionally, the new model will be manufactured with greater precision using an anodized aluminum alloy that can withstand short testing durations in a high-temperature flow.

V. Acknowledgments

Carson Waddell is supported by the US Air Force Office of Scientific Research (AFOSR) Young Investigator Award number FA9550-21-1-0183 monitored by Dr. Amanda Chou. The authors gratefully acknowledge this source of support. The authors also wish to express their gratitude to Mr. Killian Samuels for providing the mentorship and training necessary to complete this work.

References

[1] Settles, G. S., *Schlieren and shadowgraph techniques: visualizing phenomena in transparent media*, Springer Science & Business Media, 2001.

[2] Kennedy, R. E., Laurence, S. J., Smith, M. S., and Marineau, E. C., "Hypersonic boundary-layer transition features from high-speed schlieren images," *55th AIAA Aerospace Sciences Meeting*, 2017, p. 1683.

[3] Boselli, M., Colombo, V., Ghedini, E., Gherardi, M., Laurita, R., Liguori, A., Sanibondi, P., and Stancampiano, A., "Schlieren high-speed imaging of a nanosecond pulsed atmospheric pressure non-equilibrium plasma jet," *Plasma chemistry and plasma processing*, Vol. 34, 2014, pp. 853–869.

[4] Versluis, M., "High-speed imaging in fluids," *Experiments in fluids*, Vol. 54, 2013, pp. 1–35.

[5] Settles, G. S., and Hargather, M. J., "A review of recent developments in schlieren and shadowgraph techniques," *Measurement Science and Technology*, Vol. 28, No. 4, 2017, p. 042001.

[6] Arrington, A., Pastor, C., and Simerly, S., "Aerodynamic Testing Capabilities of the NASA Glenn 10-by 10-Foot Supersonic Wind Tunnel," *49th AIAA Aerospace Sciences Meeting including the New Horizons Forum and Aerospace Exposition*, ????, p. 1066.

[7] Burns, R. A., Fahringer Jr, T. W., and Danehy, P. M., "Visualization of Freestream Vortices in the NASA Langley 4-Foot Supersonic Unitary Plan Wind Tunnel," *21st International Symposium on Applications of Laser and Imaging Techniques to Fluid Mechanics*, 2024.

[8] Segal, C., *The scramjet engine: processes and characteristics*, Vol. 25, Cambridge University Press, 2009.

[9] Byrd, A., and Baccarella, D., "Design of the University of Tennessee High-Enthalpy Tunnel," *AIAA Paper 2021-0382*, 2021. https://doi.org/10.2514/6.2021-0382.

[10] Baccarella, D., and Samuels, K. E., "Characterization of University of Tennessee High-Enthalpy Tunnel with Nitrogen Flow," *Journal of Thermophysics and Heat Transfer*, 2024, pp. 1–14.